Thermodynamic characteristics and responses to ENSO of dominant intraseasonal modes in the East Asian summer monsoon

Hyoeun Oh · Kyung-Ja Ha

Abstract The moisture supply and El Niño Southern Oscillation (ENSO) characteristics are investigated for different intraseasonal modes of the East Asian summer monsoon (EASM) identified as the Meiyu–Baiu, Changma, post-Changma, and dry-spell modes. The investigation is conducted with a type of artificial neural network known as self-organizing map analysis. The major modes tend to be dominated by the moisture convergence of the moisture budget equation along the rain-band. The Meiyu–Baiu mode is strongly linked to both the anomalous low-level convergence and vertical wind shear, which is related to baroclinic instability with warm air rising and cold air sinking. The Changma mode has a strengthened tropic–subtropics connection along the western north Pacific subtropical high, which induces vertical destabilization and strong convective instability by the low-level warm advection of moisture-laden air and upper-level cold advection of dry air. In late summer, the post-Changma and dry-spell modes are characterized by anomalous southeasterly flow of warm and moist air from western north Pacific monsoon, and low-level easterly flow, respectively. In response to the preceding El Niño, the Meiyu–Baiu and Changma modes occur more frequently, while the post-Changma and dry-spell modes show the opposite. The response to the La Niña exhibits a relatively weak connection, indicating asymmetric response on the preceding ENSO. This prominent difference in response to the ENSO leads to different behaviors of the Indian Ocean and western Pacific thermal state, and consequently, the distinct moisture supply and instability variations for the EASM intraseasonal modes.

1 Introduction

The East Asian summer monsoon (EASM) is a complex mid-latitude system that produces phenomena with various spatiotemporal scales. One of the dominant variabilities in the EASM is intraseasonal variation (ISV), which is related to an irregularly propagating large-scale intraseasonal oscillation (ISO) with a period of 30–60 days (Yasunari 1979; Yun et al. 2008). There have been many efforts to identify the different spatiotemporal structures of the intraseasonal EASM. Wang and Xu (1997) found that the climatological ISO has regional differences. The primary East Asian rain-band refer to as Meiyu in China and Baiu in Japan in early June, while Changma in Korea appears from mid-June to late July. According to the Korean rainy season, the post-Changma is popularly known as a secondary surge from mid-August to early September (Ha and Lee 2007; Kim et al. 2010; Lee et al. 2010). Ha et al. (2009) demonstrated the different formation mechanisms by identifying the wave structures between the Changma and post-Changma: the Pacific-Japan pattern (Nitta 1987) in the Changma and the zonal wave-like pattern along the Eurasian continent (Enomoto et al. 2003) in the post-Changma. The different dynamics between the Changma and post-Changma suggest the importance of identifying the intraseasonal phases (ISP) of the EASM. The underlying characteristics of complex ISV may provide valuable insights that enhance the predictability of the EASM precipitation (Kim et al. 2008).

Of particular interest is that the moisture is transported from the nearby oceans to the East Asian monsoon region by

H. Oh · K.-J. Ha (✉)
Division of Earth Environmental System, Pusan National University, Busan, Korea
e-mail: kjha@pusan.ac.kr

large-scale monsoon circulations and it plays a key role in modulating the ISP (i.e., onset and withdrawal) of the EASM (Zhou and Yu 2005). Seo et al. (2012) demonstrated that the extraordinary northwestward intensification of the North Pacific subtropical high induces the strong southerly winds, leading to large amount of precipitation over the EASM region. In order to better understand the processes that generate precipitation, it is important to confirm more quantitative manner on decomposition analysis using moisture budget equation by mean and transient parts. The moisture budget studies have been widely known over the recent decade. For example, Zhang et al. (2011) tried to show the moisture divergence by dividing into the monthly-wind moisture transport (MMT) and transient eddy moisture transport (EMT) divergence. They revealed that the MMT represents strong moisture convergence in the EASM region, while the EMT divergence has the opposite effect on the MMT. Moreover, the primary causes of the increasing precipitation were investigated by analyzing the structures related to atmospheric moisture budget (Li et al. 2013). Hence, understanding of the progress of moisture supply requires detailed analysis of the atmospheric moisture budget.

In previous studies, it has been discovered that scale interactions between intraseasonal and interannual variability (IAV) determinate the predictability sources based on surrounding factors. Yun et al. (2008) found that the boreal summer northward propagating ISO over the EASM region is affected by the preceding El Niño Southern Oscillation (ENSO). They also reported that one of the possible linkages is related to the springtime SST warming over Indian Ocean (IO) via Walker circulation. The warming induces a suppressed convection and an anomalous western north Pacific subtropical high (WNPSH) over the Philippine Sea, further, it leads to Rossby wave train over the EASM region. Lee et al. (2013b) indicated that the moisture convergence is simultaneously enhanced by inducing impact of more evaporation through anomalous SST warming over the IO. The moisture supply over East Asia is also related to external forcing such as the ENSO through the modulation of an anomalous WNPSH (Huang and Wu 1989; Wang et al. 2000, 2013; Chou et al. 2003; Lee et al. 2013a; Yun et al. 2013). The anomalous WNPSH is attributed to local air-sea interactions, the influence of the IO, and the combined effect on atmospheric circulation (Ashok et al. 2001; Saji and Yamagata 2003; Xie et al. 2009; Lee et al. 2013b; Yun et al. 2013). The different ISO-ENSO relationship between early and late summer has been shown in Teng and Wang (2003): the eastward propagating in early summer and the northward propagating in late summer. Recently, Karori et al. (2013) showed that two different features of the ENSO, namely, the warm pool and cold tongue ENSO, produce an asymmetric atmospheric Rossby wave response that results in opposite precipitation

anomalies over the EASM. Hence, it would be useful to investigate the linkage between the IAV of the ISP and the ENSO with the seasonal evolution to understand influence of tropical SST as predictive factor.

The intraseasonal characteristics of the EASM have been typically approached by statistical methods based on linear analyses (Kang et al. 1999; Zhou and Yu 2005). However, these linear analyses have a limited ability to capture the characteristics of the intraseasonal monsoon variation (Yoo et al. 2010). Johnson (2013) classified the difference between k-means clustering and self-organizing map (SOM) to compare the results. Both two methods are very similar, but only SOM has a neighborhood function to preserve the topological ordering when modifying centroids vectors. The SOM, which has no constraint for linearity or orthogonality, can provide effectively various extractions. Recently, Chu et al. (2012) used a nonlinear analysis of SOM to identify four major ISP of the EASM named as the Meiyu–Baiu mode, Changma mode, post-Changma mode, and dry-spell mode and investigated their dynamical structures. The study focused on the adoption of SOM methodology and proved the strength of SOM for isolating the nonlinear coupled states. In addition, by using the annual number of clustered days, they found that particular monsoon phases are more favorable to the ENSO. However, the different thermodynamic structures and moisture supplies for the four ISP of the EASM were not undertaken. The seasonal evolution of the tropical sea surface temperature (SST), which reflects the phase transitions and detailed characteristics of the asymmetric response to the ENSO, was not considered as well. In this study, we explore moisture supplies, thermodynamic structures, and mechanisms of the major ISP identified by Chu et al. (2012), but the analysis period is extended to 2012. For the moisture analysis, we adopt the moisture budget equation including convergence, advection, and transient eddies. We also demonstrate that prominent differences in moisture supply and instability are caused by distinct responses to the preceding ENSO. Section 2 briefly explains the main ideas behind the implementation of SOM and the identification of the four major modes. Section 3 identifies the moisture supply of the four major intraseasonal modes. In addition, the thermodynamic structure is examined in terms of instability. Section 4 demonstrates the different influences of the preceding ENSO, and Sect. 5 contains a summary as well as conclusions.

2 Data and methods

2.1 Datasets for SOM and SST

To identify the major intraseasonal modes of the EASM, a type of artificial neural network known as SOM was

applied (Appendix). The input data consisted of the daily standardized anomalies of the six monsoon indices by earlier researchers (e.g., CI500H, CI850U, and CI850V indices (Ha et al. 2005), RM2 index (Lau et al. 2000), SI index (Wang et al. 1998), and the western North Pacific monsoon index (WNPMI) (Wang et al. 2001)) representing large-scale changes in the WNPSH, low-level winds, upper-level vorticity, vertical shear of zonal wind, and the intensity of the low-level vorticity for the period from 1979 to 2012, but we carried out the experiment with fixed reference vectors in Chu et al. (2012). This is because we expect that the dynamical results are equivalent to previous studies. Seasonal variations of each monsoon index selected were relatively independent of the others. In order to confirm the robustness of SOM, the sensitivity test was examined by removing each index [refer to Chu et al. (2012)]. Even though one index was removed, they could capture the four dominant modes as a result. The data were obtained from the National Centers for Environmental Prediction/Department of Energy (NCEP–DOE) (Kanamitsu et al. 2002). The SST data for the period 1979–2012 were obtained from the Hadley Centre Sea Ice and Sea Surface Temperature dataset (HadISST), which was made available by the British Atmospheric Data Centre (BADC) (Rayner et al. 2003). The anomalies of all variables were calculated based on 1979–2012 daily climatology.

2.2 Implementation of SOM

In SOM analysis, there are two types of dimensional arrays, which consist of rectangular and hexagonal lattices. In the rectangular and hexagonal lattices, each node has four and six neighborhoods if the radius is one. We used a Gaussian neighborhood for the neighborhood kernel and rectangular lattice for dimensional array. When the type and number of the map are decided upon, the map must be kept small but sufficiently large enough to express the different characteristics of the input data (figure not shown). Thus, the value of 3×3 was chosen to be captured on SOM based on requirement of mathematical and physical optimizations of identifying distinct patterns. The final map considers the mean spatial patterns in the EASM characterized by active, break, and normal conditions, including both major and subsequent modes (Chattopadhyay et al. 2008). The standardized anomalies of the six monsoon indices [e.g., CI500H, CI850U, and CI850V indices (Ha et al. 2005), RM2 index (Lau et al. 2000), SI index (Wang et al. 1998), and the WNPMI (Wang et al. 2001)] were arranged as input vectors. Each of the 92 days (from 1 June to 31 August) and each of the 34 years (from 1979 to 2012) were associated with a particular node of the 3×3 map; 3,128 input samples (92 days $\times$ 34 years) were analyzed. On the basis of greater portion and sustainability of the ISP identified

Table 1 Mean days per event (in boldface), frequency of days in percent (in parentheses), and probability of no transition at each node (in braces)

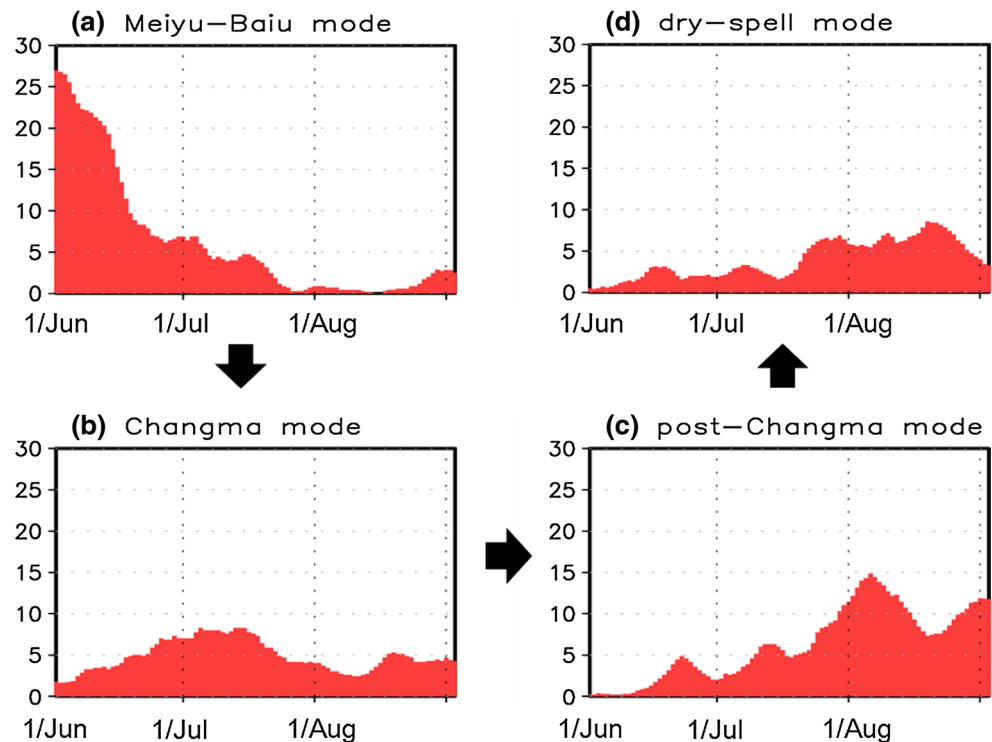| Meiyu–Baiu mode	Dry-spell mode
6 (18.8 %) {79.5}	**4** (11.8 %) {67.6}
Changma mode	Post-Changma mode
4 (14.3 %) {69.1}	**5** (18.6 %) {74.9}

by SOM, four dominant modes located at the far corners of 3×3 map were considered as dominant modes [The figure of 3×3 map can be found in Chu and Ha (2011)]. The dominant modes can explain an episode because they are relatively stationary.

2.3 Identification of dominant modes

To provide basic statistical information on the phases, we listed the mean days per event, frequency of days in percent, and probability of no transition from one mode to another in Table 1. The number of events was determined by counting the total number of each mode. The mean days per event was calculated by averaging the number of clustered event days per year. The percentage frequency of days was calculated by taking the number of clustered days in a particular mode and dividing the number by the total number of days (3,128 days = 92 days year^{-1} $\times$ 34 years), and then the results were multiplied by 100 to convert the ratio into a percentage. The probability of no transition is the probability that any consecutive days regarded as input vectors will be mapped to the same mode. The mean days per event had a maximum of 6 days for the Meiyu–Baiu mode occupied by 18.8 % of the EASM. Furthermore, the probability of no transition the next day was 79.5 %, which was the highest probability of clustering at the equal mode. The frequency of days was occupied by 18.6 % in the post-Changma mode. For the Changma mode and dry-spell modes, 14.3 and 11.8 % were projected, respectively. The four dominant modes that occupied about 63.5 % of the EASM were selected by the analysis.

Figure 1 shows the number of clustered days in each major mode in June–July–August (JJA) for the 34 year period. 7-day running average is applied. By averaging on 7 days, we could find concentrated peaks of each mode representing their seasonal variation. According to Fig. 1, SOM effectively captured temporal information on the climatological intraseasonal phases (CISP). The counterclockwise direction depicts the evolution of the four modes starting from the Meiyu–Baiu mode. The Meiyu–Baiu mode appeared in early summer, and then the Changma mode emerged from late June to early July. The post-Changma mode had its maximum peak in early August and

the dry-spell mode manifested during late summer. Thus, we could find that the CISP are different.

Moreover, the IAV of four major modes is defined by the mean annual number of days clustered at each mode. The IAV of the Meiyu–Baiu mode showed no significant correlation with that of the Changma mode (correlation coefficient of -0.02). It confirmed that SOM have the ability to classify the Meiyu–Baiu and Changma modes, which occur during early summer and both two modes are independent each other. On the other hand, the post-Changma and dry-spell modes were negatively correlated to the Meiyu–Baiu and Changma modes in at the 99 % confidence level and the correlation coefficients were -0.52 and -0.53, respectively.

## 3 Moisture transport and instability

3.1 Moisture transport

The northward-propagating ISP, which evolve in the counterclockwise direction starting from (a–d) along peak time for each mode, can be seen in Fig. 2 (Wang and Xu 1997; Yun et al. 2009). A full cycle with counterclockwise direction of the ISP is an episode elsewhere (Chu et al. 2012). The vertically integrated moisture flux convergence anomaly represents some identified aspects of thermodynamic and dynamic effects on precipitation systems. In this section, we focus on the distinctive moisture supply for each

mode. Figure 2 shows the spatial distribution of the vertically integrated moisture flux convergence anomaly and moisture transport at 925-hPa by the anomalous low-level wind associated with SOM classified patterns. In the Meiyu–Baiu mode, the anomalous cyclonic circulation at the low-level induces a strong moisture flux convergence on the precipitation region over southern Japan. Such a zonally elongated concentration of anomalous moisture flux convergence can easily make conditions favorable to precipitation. In contrast, an anomalous moisture flux divergence appears over the South China Sea and the eastern north Pacific.

The Changma mode shows prominent WNPSH and it leads to stronger southwesterly moisture transport from the subtropics to East Asia. The southwesterly flow due to the WNPSH plays an important role as a source of moisture. The contrast between the convergence in the tropics and divergence in the subtropics is more evident than the Meiyu–Baiu mode. It implies that the Changma mode has more to do with the tropical thermal state. In addition, another evidence of a connection with the equator can be found in the easterly vertical wind shear between 200- and 850-hPa related to the northward propagating ISO (figure not shown).

The post-Changma mode is diagonally opposite to the Meiyu–Baiu mode (Chu and Ha 2011). The strong moisture flux convergence anomaly related to enhanced deep convection over the western north Pacific (WNP) can explain the emanation of Rossby waves, which is

Fig. 2 Spatial distributions of vertically integrated moisture flux convergence anomaly (*shading* unit: mm day^{-1}) and moisture transport anomaly at 925-hPa (vector, unit: m s^{-1}) for **a** Meiyu–Baiu, **b** Changma, **c** post-Changma, and **d** dry-spell modes (above 0.01 m s^{-1}). *Green shading* means moisture flux convergence, while *yellow shading* indicates divergence
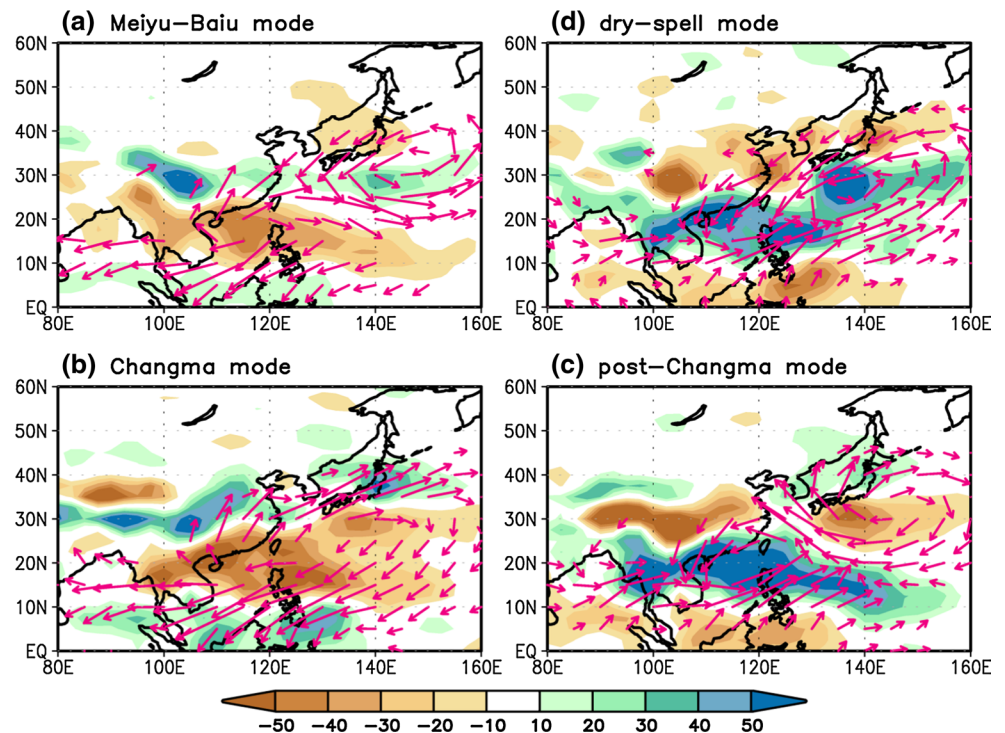
indicative of the northward propagating ISO (Kemball-Cook and Wang 2001; Tsou et al. 2005). As a result, this mode has the persistent wavelike structure to explain Rossby wave propagation for large-scale circulation conspicuously. The anomalous anticyclone in the Changma mode seems to advance northward to southern Japan in this mode. For the reason, the Korean Peninsula is affected by the southeasterly flow along the anomalous anticyclone over southern Japan. From different standpoints, there are two phenomena in the subtropics. One is the western north Pacific summer monsoon (WNPSM) associated with cross-equatorial flows such as the Somali jet that supplies massive moisture (Wang et al. 2001). The other is the typhoon effect in August. The evidence is the precipitation distribution associated with the track of the tropical cyclone (TC) motion and the increasing trend of the IAV related to TC activity in the late-1970s, concurred with Kwon et al. (2007). Thus, this mode is conjunct with various phenomena be found during late summer.

The dry-spell mode features a mirror phase of the Changma mode. This mode has approached by the anomalous cyclonic circulation over the WNP region. The anomalous easterly flow at the low-level near southern Japan terminates the moist supply into the EASM. Hence, the EASM regions experience dry conditions. The dry conditions in this mode are significantly related to the Eurasian wave-like pattern descried in Ha et al. (2009).

3.2 Moisture budget analysis

To better estimate the contribution of moisture supply, we applied the moisture budget equation on decomposition analysis (Appendix). According to Seager et al. (2010), the final equation can be written as

$$\rho_w g(P - E) \cong -\int_0^{P_s} \left(\overline{q}\nabla \cdot \overline{V} + \overline{V} \cdot \nabla\overline{q}\right)dp - \int_0^{P_s} \nabla \cdot \left(\overline{V'q'}\right)dp \qquad (1)$$

where the overbars indicate 15-day running means for each year and the primes indicate departures from the 15-day running means. We can consider the prime terms as transient eddy terms. The first term on the right-hand side of Eq. (1) represents the moisture convergence as a dynamic term, and the second term represents the moisture advection as a thermodynamic term. The third term represents the transient eddy moisture flux convergence as a transient term.

Here we queried how much does each term contribute to the major ISP in the EASM? By making comparison to identify which term is dominant, we expect to find features of the moisture supply in the EASM quantitatively. The moisture budget equation is separated into terms of the anomalous moisture convergence, moisture advection, and transient eddy moisture fluxes (Figs. 3, 4, 5). All four modes are dominated by the anomalous moisture convergence term (Fig. 3). The Meiyu–Baiu mode has a zonally elongated convergence region from eastern China to the

Fig. 3 Spatial distributions of the anomalous convergence term (mm day^{-1}) in the moisture budget equation for **a** Meiyu–Baiu, **b** Changma, **c** post-Changma, and **d** dry-spell modes
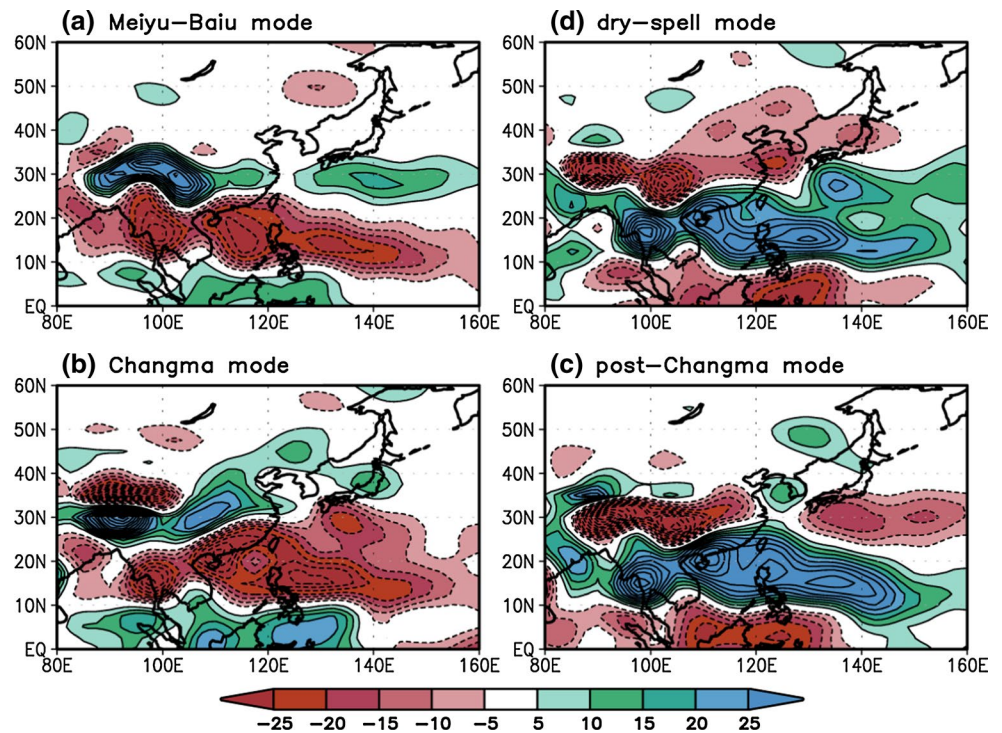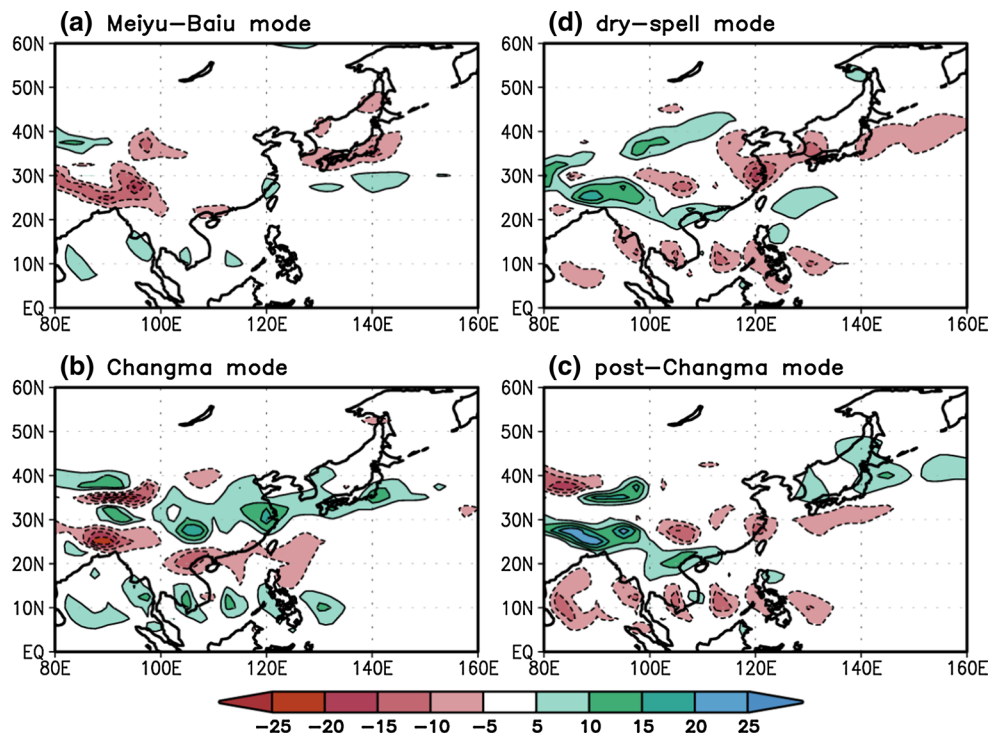

Fig. 4 Same as Fig. 3, but for the anomalous advection term

southern Japan and a divergence region on a subtropical high. In Changma mode, the anomalous convergence region is displayed as a diagonal line near the Korean Peninsula. This is because the mode has vertical structures that include anomalous moisture flux convergence

at the low-level and divergence at the middle-level over the Korean Peninsula (Fig. 6b). In addition, the covering a larger divergence region implies that there is a strengthened subtropical high over the western Pacific (WP) in the Changma mode (Fig. 3b). Both the post-Changma and

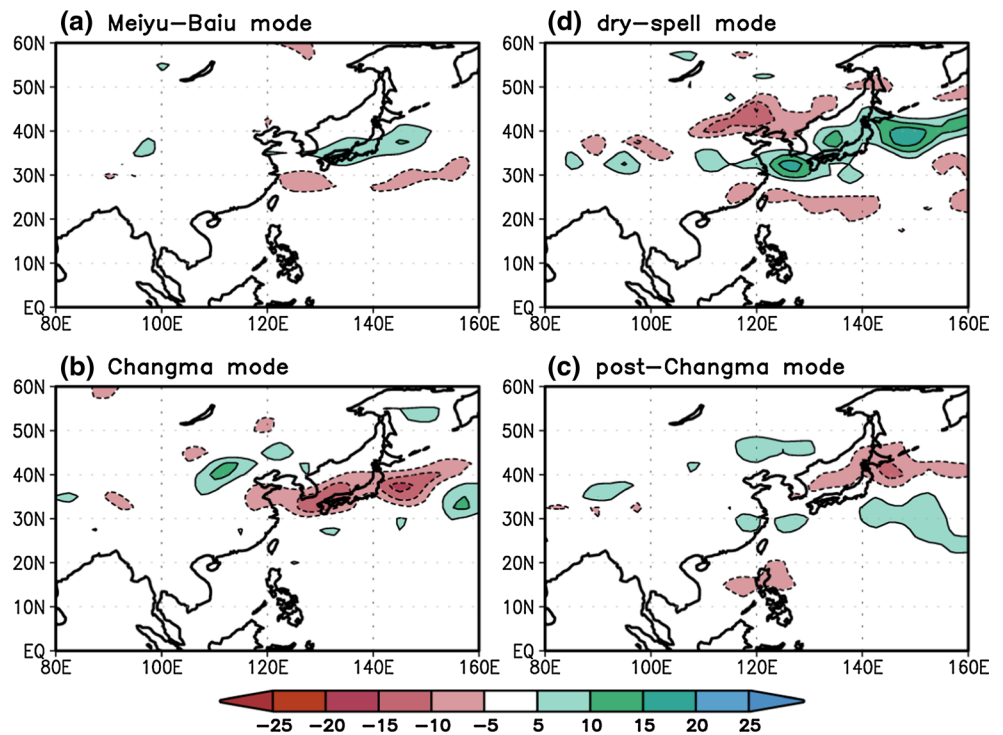**Fig. 5** Same as Fig. 3, but for the transient eddy term

Fig. 6 Latitude–height cross sections of both the moisture flux convergence (*shading* unit: day^{-1}) and thermal advection anomalies (*contour* unit: K day^{-1}) for **a** Meiyu–Baiu, **b** Changma, **c** post-Changma, and **d** dry-spell modes averaged over the longitude (120°–140°E). *Green shading* means moisture flux convergence, while *yellow shading* indicates divergence. *Red solid* and *blue dashed lines* represent warm and cold advections, respectively. The *shading* and *contour* intervals are 2.0 and 0.1, respectively
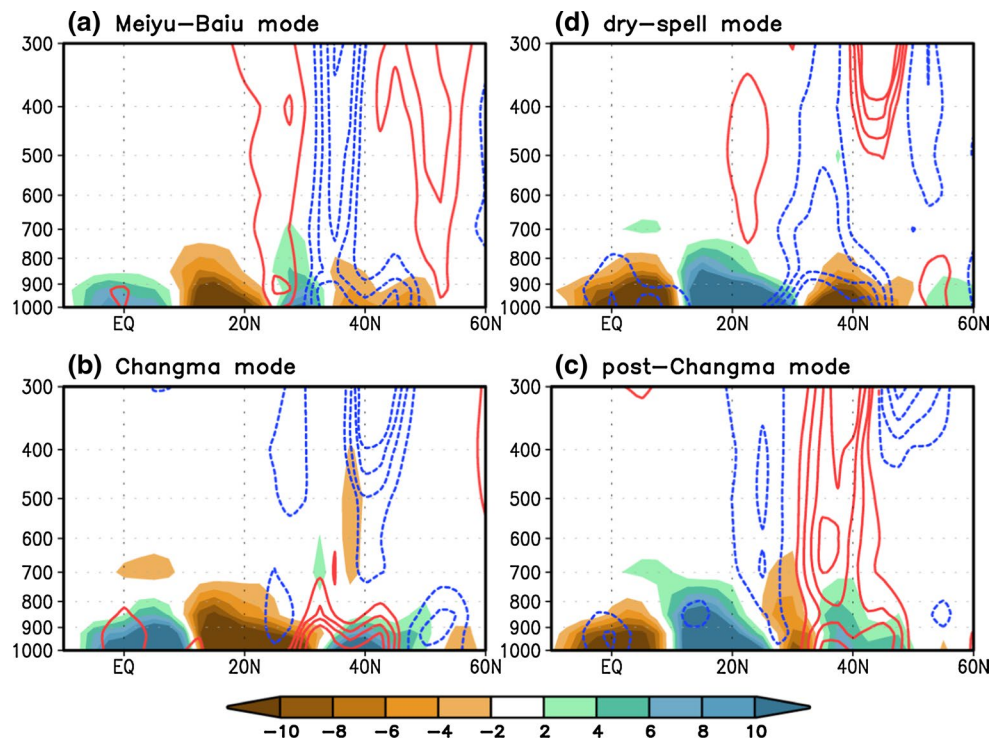
dry-spell modes also display conformity of the anomalous moisture flux convergence over the precipitation region (Fig. 3c, d). The anomalous convergence located over the WNP is characterized by more active convection than that over the EASM region in both of the two modes.

The anomalous advection term plays an important role in the identification of modes (Fig. 4). In the Changma mode, the considerable contribution of the anomalous advection term can explain localized rainfall over the Korean Peninsula. This analysis reveals that the Changma mode

Fig. 7 Latitude–height cross sections of both the vertical (*shading* unit: Pa s^{-1}) and zonal winds (*contour* unit: m s^{-1}) for **a** Meiyu–Baiu, **b** Changma, **c** post-Changma, and **d** dry-spell modes averaged over the longitude (120°–140°E)
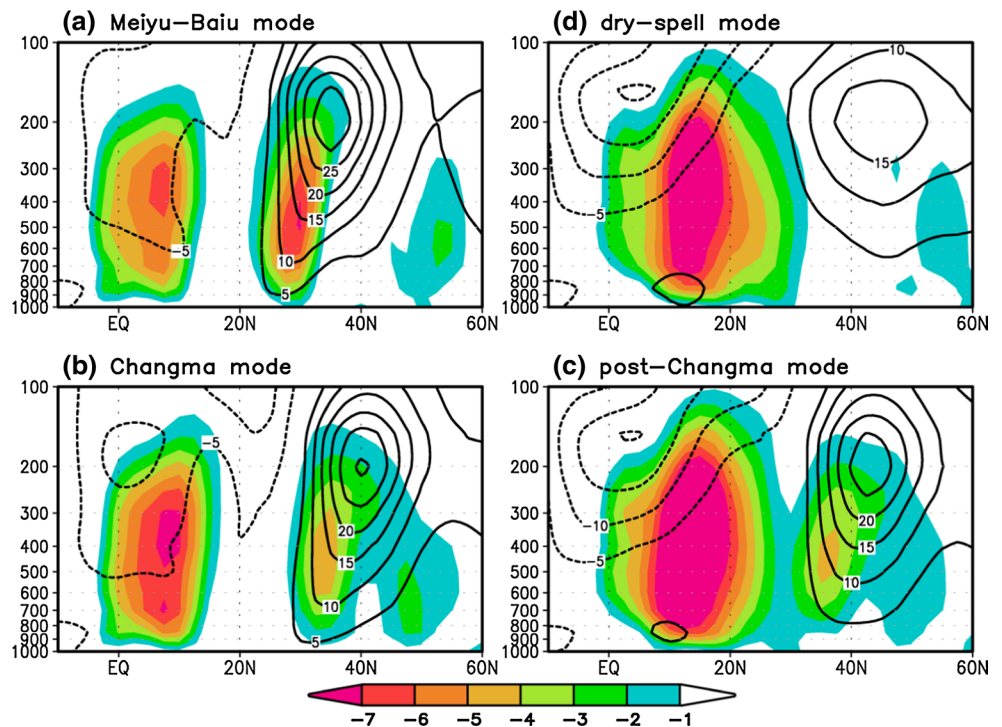
is mostly affected by the anomalous southwesterly wind that involves a large amount of moisture from the subtropical region along the WNPSH. That is the reason why the Changma mode can be distinguished from the Meiyu–Baiu mode (Fig. 4a, b). The other reason is that the two modes have the distinct center in the vertical structure of specific humidity each other. The center of specific humidity in the Meiyu–Baiu mode is located at 700-hPa, while that in the Changma mode is more concentrated at the low-level. This implies that the Changma mode is controlled by warm rain convection or a "low-echo centroid" precipitation system, which does not generate lightning (Sanjib and Ha 2003). In addition, the flow caused by the contrast between dry land and humid ocean is also prominent over southern Korea in the Changma mode (figure not shown). Note that the land-sea contrast between dry land and humid ocean leads to the meridional wind component with warm-damp air. A mirror image of the Meiyu–Baiu mode is observed in the post-Changma mode (Fig. 4c). Thus, as the result of the Meiyu–Baiu mode, the advection term has no particular importance. However, in dry-spell mode, the negative advection covers the EASM region (Fig. 4d). For this reason, this mode leads to beginning of dry weather over the EASM region.

The distinct characteristics are also exhibited by the anomalous transient eddy flux convergence term (Fig. 5). The anomalous transient eddy term in summer is smaller than winter because transient wave activity weakens rapidly from spring to summer (Nakamura 1992). In all four

modes, the anomalous transient eddies have the opposite phase by supplying or blocking moisture over the boundary region of the mean flow and their role is smaller than the moisture flux convergence (Zhang et al. 2011). In other words, the transient eddy divergence (convergence) is observed to influence a decrease (an increase) in rainfall (Zhang et al. 2011).

3.3 Instabilities

The instability associated with the dominant modes will be examined in terms of the thermodynamic and dynamic factors. As the thermodynamic factors, the vertical structure of moisture flux convergence and thermal advection are examined (Fig. 6). As the dynamic factors, the zonal and vertical winds are considered (Fig. 7). In addition, the remarkable difference in instabilities is further investigated by focusing on two modes, which occur during early summer, corresponding to the Meiyu–Baiu and Changma modes (Fig. 8). First, the Meiyu–Baiu mode has an obvious boundary where the thermal gradient corresponds to warm and cold advection to the south and north of the whole atmosphere, respectively. The meridional thermal gradient results in the upper-level jet stream. Warm air is confined to the subtropics, cold air is confined to mid-latitudes, and strong westerly wind shear is shown over the same region (Figs. 6a, 7a). The strong jet stream makes the ascending motion strengthen. It means there is a strong secondary circulation over the warm advection region in this mode, whereas the

Fig. 8 Spatial distributions of the 200 hPa zonal wind (*black contour* unit: m s^{-1}), Eady growth rate between 400- and 600-hPa (*shading*), and 5,880-gpm contour (*red line*) for **a** Meiyu–Baiu and **b** Changma modes (*left panel*) and *right panel* is for longitude–height cross sections of the vertical gradient of equivalent potential temperature anomaly (K hPa^{-1}) meridionally averaged for **c** Meiyu–Baiu (20°–30°N) and **d** Changma modes (30°–40°N) (*right panel*)
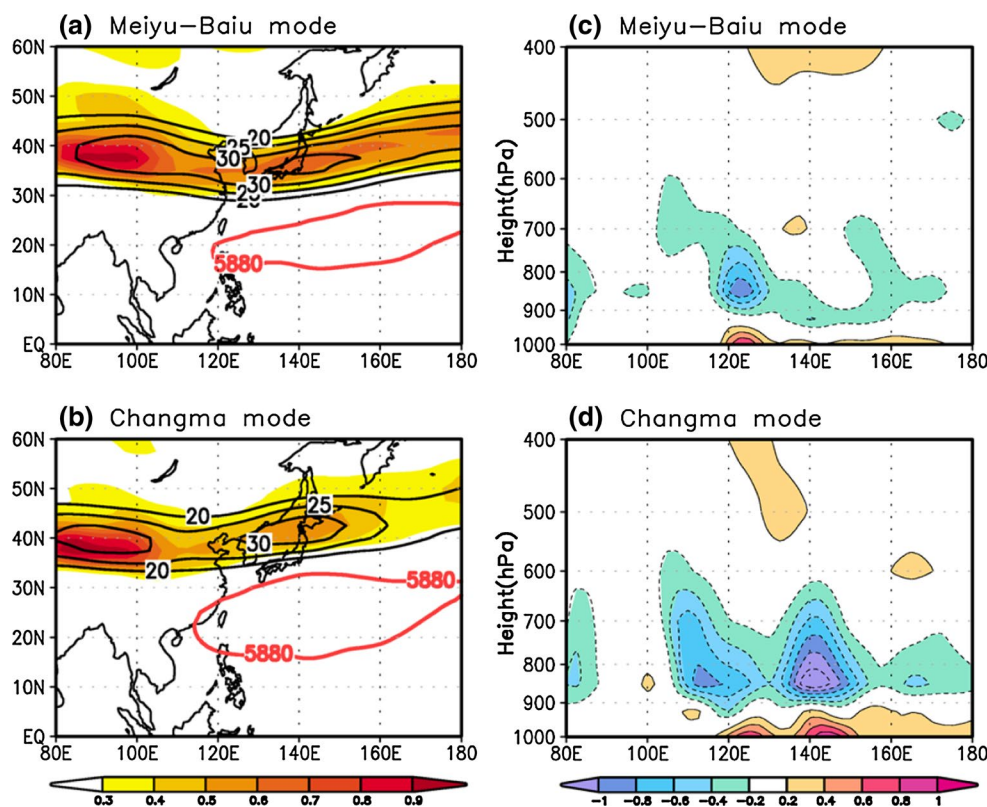
Changma mode is not. The vertical shear of the mean flow is associated with baroclinic instability converting potential energy. The Eady growth rate between 400- and 600-hPa shows a much stronger response than the Changma mode. The maximum Eady growth (Lindzen and Farrell 1980), which is directly linked to the meridional thermal gradient, is one of simple paradigms for the instability (Fig. 8a, b). In addition, the Meiyu–Baiu mode has a feeble moisture flux convergence anomaly and weak ascending motion on the equator. The mode may be more connected by the mid-latitude system related to the jet stream than the tropical system.

The vertical structures are composed of an anomalous moisture flux divergence at the middle-level and convergence at the low-level in the Changma mode (Fig. 6b). The dynamical characteristics are shown in Fig. 7b. The weak secondary circulation results from weak upper-level jet stream to be extended northward. The moisture structures with thermal advection are principal factors for the generation of convective instability. The anomalous warm advection occurs mainly at the low-level from the south through the established WNPSH, while the anomalous cold advection occurs at the upper-level from the north. Under this condition, the warm advection can meet over the moisture flux convergence region at the low-level. That is why convective instability develops in the Changma mode. Convective instability is characterized

by warm moist air at the low-level and cold dry air at the upper-level. The evident increase in convective instability is represented by much moisture at the lower level (Fig. 6b) (Yun et al. 2008). The Changma mode remarkably exhibits the vertical gradient of the equivalent potential temperature indicating the convective instability than the Meiyu–Baiu mode (Fig. 8c, d). Furthermore, the Changma mode has a strong moisture flux convergence anomaly, obvious ascending motion on the equator, and significant easterly wind shear between 200- and 850-hPa (figure not shown). The easterly wind shear provides some information about the northward propagation of tropical activity from the subtropical region, including convective activity (Jiang et al. 2004). Thus, we can observe that the Changma mode has much stronger linkages to the subtropical region than the Meiyu–Baiu mode.

The post-Changma mode is influenced by warm advection in the whole atmosphere as in the Meiyu–Baiu mode (Fig. 6c), but has the center of specific humidity concentrated at the low-level as it was in the Changma mode (figure not shown). In other words, this mode has intermediate features between the Meiyu–Baiu and Changma modes in the mid-latitudes. The easterly wind shear can also explain the development of the northward propagation in the subtropics (Fig. 7c). From different point of view, the strong upward motion in the subtropics is characteristic of the WNPSM. This feature is associated with the WNPSM with

the strong moisture flux convergence over the same region as we mentioned.

In the dry-spell mode, an anomalous cold advection over anomalous moisture flux divergence region is located in the EASM region (Fig. 6d). Both of the anomalous cold advection with dry air at the low-level and warm advection at the upper-level provide vertical stabilization. This process creates dry conditions over the EASM region. In addition, the secondary circulation in the mid-latitudes is very weak in this mode due to the weak jet stream. Over the WNP region, both a strong moisture flux convergence anomaly and upward motion develop, similar to the post-Changma mode.

4 Asymmetric response to ENSO

The prominent differences in response to moisture supply and instability in the dominant modes may be caused by distinct responses to the preceding ENSO. Many previous studies have been performed to examine the relationship between tropical Pacific SST and the East Asian monsoon (Chang et al. 2000; Wang et al. 2000; Wu et al. 2003). Chu et al. (2012) also found that the ISP can be controlled by the external components such as the ENSO. However, the linkage between the ISO in the EASM and ENSO has not been clearly revealed due to different time and space scales. The possible linkage between the IAV of the northward propagating ISO in the EASM and quasi-biennial-type ENSO was suggested to relate to the reinforced WNPSH by Yun et al. (2009). To examine how the dominant modes are influenced by the preceding ENSO based on a classifying algorithm, we need to consider responses to the ENSO and the seasonal evolution of the tropical SST that indicate detailed transitions and characteristics.

Firstly, indications of responses to ENSO are constructed by the changes in the number of occurrence on interannual time scales during El Niño and La Niña years. To demonstrate the impact of the preceding ENSO on the dominant ISP, we used a time series of the mean annual number of days per event. We selected 10 El Niño years and 14 La Niña years by adding five El Niño years in the previous study [refer to Chu et al. (2012)]. El Niño years—1983, 1987, 1988, 1992, 1995, 1998, 2003, 2005, 2007, and 2010 and La Niña years—1984, 1985, 1986, 1989, 1996, 1997, 1999, 2000, 2001, 2006, 2008, 2009, 2011, and 2012. The definition of the ENSO years was based on a threshold of ±0.5 °C for the December–January–February (DJF) Niño-3.4 index with a 3-month running mean of SST anomalies in the Niño-3.4 region (5°N–5°S, 120°–170°W). According to the ENSO dependence, the mean number of days for the El Niño event increased in the Meiyu–Baiu and Changma modes by 28.6 and 42.2 %, respectively (Table 2). This

Table 2 Variations in the number of days for (a) Meiyu–Baiu, (b) Changma, (c) post-Changma, and (d) dry-spell modes associated with preceding ENSO

Type	Mode			
	(a) Meiyu–Baiu mode (%)	(b) Changma mode (%)	(c) Post-Changma mode (%)	(d) Dry-spell mode (%)
After El Niño	28.6	42.2	−26.4	−52.9
After La Niña	1.8	−23.9	6.8	17.5

indicates that the Meiyu–Baiu and Changma modes which occur during the early summer are stimulated by the preceding El Niño events. In contrast, the mean number of days for the El Niño event decreased in the post-Changma and dry-spell modes by 26.4 and 52.9 %, respectively. That is, those modes were also affected by the preceding ENSO, but in a reverse sense. There was a little association observed between the La Niña and the Meiyu–Baiu mode (1.8 %) or the post-Changma mode (6.8 %). However, the Changma mode (dry-spell mode) tended to arise less (more) frequently through winter eastern Pacific (EP) SST cooling.

Why do the dominant modes have likely an asymmetric response to the preceding ENSO? One of the possible linkages is related to the springtime SST warming over IO via Walker circulation. The warming induces a suppressed convection and an anomalous WNPSH over the Philippine Sea, further, it leads to Rossby wave train over the EASM region. Wang et al. (2000) determined that the WP and IO SST are known to have a connection with the WNPSH, even though the IO SST is not significantly related to the WP SST. Moreover, they found that the prominent effect of the anomalous SST cooling over the WNP region can be described by positive thermodynamic feedback. Yun et al. (2013) also suggested that the IO warming and WP cooling are responsible for WNPSH variability. The tropical IO warming is an effective system into the EASM (Watanabe and Jin 2002; Xie et al. 2009). The result is on the basis of the capacitor hypothesis, which means the analogy of a battery charging a capacitor (Yang et al. 2007; Xie et al. 2009).

With regard to the seasonal evolution, the correlation maps between SST from DJF(−1) to JJA(0) and the IAV of each mode are shown in Fig. 9. The IAV of four major modes is defined by the annual number of clustered days at each mode. We found that the WNPSH variability is the key to modulate the asymmetric response to the ENSO. The results were verified by the lead-lag correlations among annual number of clustered days in the four modes and the difference between the IO and WP thermal states (figure not shown). These results are quite similar with those
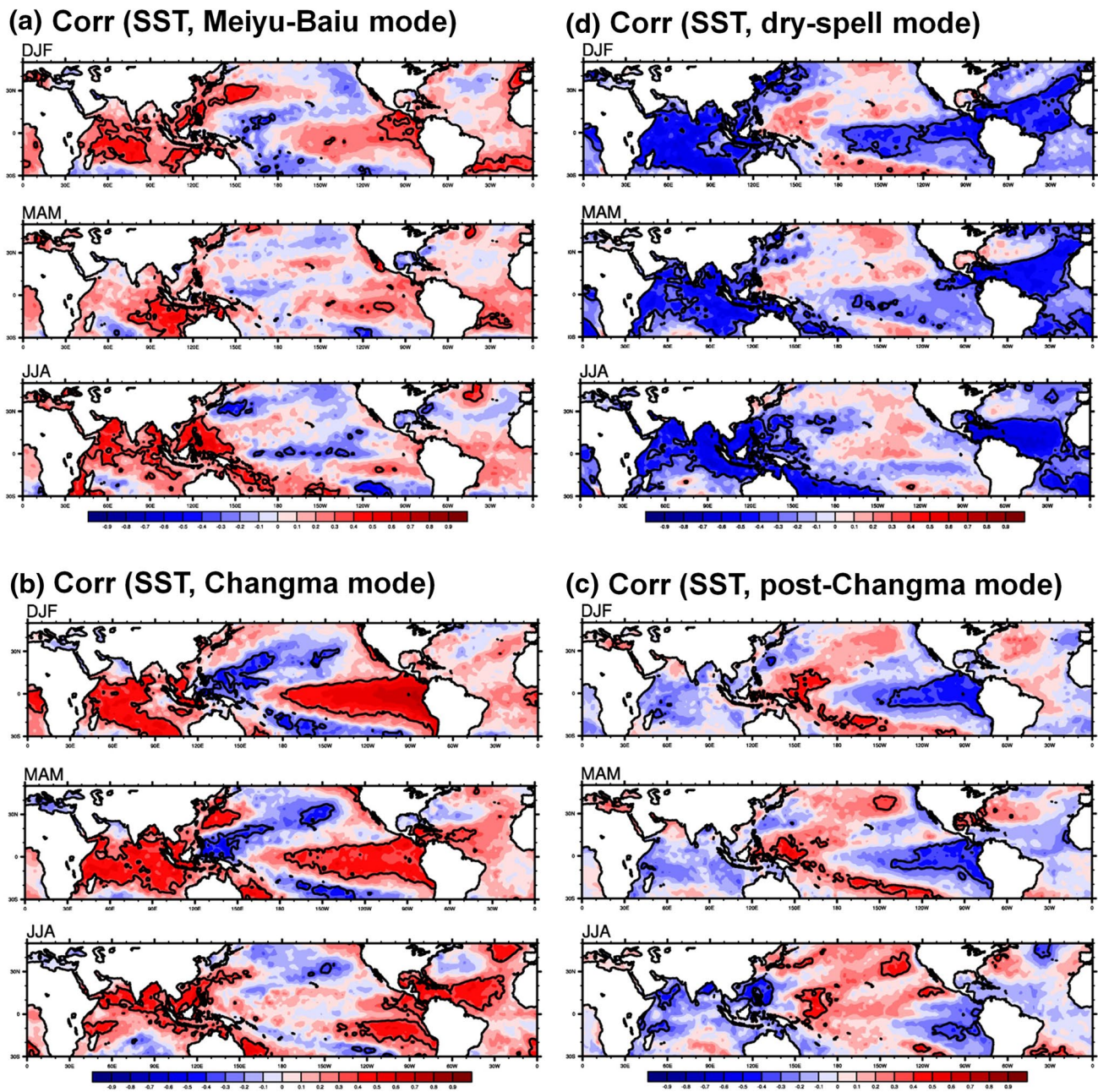
Fig. 9 Spatial patterns of the correlation coefficients with SST (December–January–February, March–April–March, and June–July–August) for **a** Meiyu–Baiu, **b** Changma, **c** post-Changma, and **d** dry-spell modes. Contour is significant at the 95 % confidence level

of Wang et al. (2013). The Meiyu–Baiu mode is weakly related with the preceding El Niño pattern. The abrupt transition of the ENSO phase in this mode is caused by the upwelling in connection with an oceanic Kelvin wave. Moreover, the anomalous anticyclone over the South China Sea corresponds with the central Pacific cooling during JJA (cf. EOF-2 in Wang et al. 2013). Conversely, the Changma mode is significantly correlated to the EP, IO, and WP SST. It can explain that the mode is very sensitive to the seasonal evolution of the ENSO through IO SST warming as well as

WP SST cooling. In the Changma mode, the northeasterly flows reinforce the mean easterlies to the southeast of the WNPSH (cf. EOF-1 in Wang et al. 2013). These flows produce SST cooling over the WP region, and then generate descending Rossby waves. In addition, the post-Changma and dry-spell modes are both related to the La Niña events, however, only the post-Changma mode represents the obvious SST warming in the WP. A conspicuous feature to be considered is a significantly negative region throughout the IO and into the Atlantic Ocean in the dry-spell mode.

Table 3 Variations in the number of days for (a) Meiyu–Baiu, (b) Changma, (c) post-Changma, and (d) dry-spell modes associated with strong or weak WNPSH years

Type	Mode			
	(a) Meiyu–Baiu mode (%)	(b) Changma mode (%)	(c) Post-Changma mode (%)	(d) Dry-spell mode (%)
Strong WNPSH	11.7	71.7	−27.6	−73.6
Weak WNPSH	−2.5	−51.6	39.2	41.7

These two modes, which are positively affected by the preceding La Niña, will be explored in the near future in detail. The atmospheric circulation patterns show the asymmetric structure, which demonstrates the asymmetric relationship between the dominant modes and the ENSO. The differences of the dominant modes can be verified by analyzing strong and weak WNPSH years (Table 3). The WNPSH index defined by Lee et al. (2013b) was used. The WNPSH index described was associated with the IAV of summer mean geopotential height at 850-hPa (110°–150°E, 15°–30°N). The definition of strong and weak WNPSH years was based on a threshold of 1.0 and −1.0 for the JJA season, respectively. For the representative strong and weak years, we selected seven strong years—1980, 1983, 1987, 1995, 1998, 2003, and 2010—and 6 weak years—1984, 1985, 1986, 2001, 2002, and 2012. The WNPSH have relevant differences to the dominant modes, especially, between the Meiyu–Baiu and Changma. It is interesting to remark that the mean number of days for the strong WNPSH years increased in the Meiyu–Baiu and Changma mode by 11.7 and 71.7 %, respectively. On the contrary, these results decreased in the post-Changma and dry-spell modes by 27.6 and 73.6 %, respectively. For the weak WNPSH years, the Changma and dry-spell modes are significantly decreased and increased, respectively. Thus, the Changma and dry-spell modes are greatly influenced by the WNPSH variability, caused by the IO warming and WP cooling. In this study, the distinct responses to ENSO in the dominant modes are remarkably consistent with the results in the Wang et al. (2013), even though we make use of a clustering method as SOM. It means that the dominant modes classified by SOM method have the possibility representing the seasonal characteristics.

5 Summary and conclusions

The thermodynamic characteristics in the intraseasonal EASM phases were examined to overcome limitations of the linear analysis and to understand the modulation by the preceding ENSO. In contrast with the linear techniques, SOM had the capability of identifying ISP in the EASM including their evolutionary histories (Chattopadhyay et al. 2008; Chu et al. 2012; Johnson 2013). We adopted

SOM analysis to fully capture the spatial and temporal characteristics of the ISP in the EASM. Chu et al. (2012) established the four dominant modes located at the far corners of 3 × 3 map and revealed their dynamical structures. In this study, we aimed to describe the uniqueness of moisture supply and demonstrated the distinct instability in terms of their dynamical and thermodynamic structure according to the major ISP identified by Chu et al. (2012). Furthermore, their asymmetric responses to the ENSO were explored as well. On the basis of greater portion and sustainability of the ISP classified by SOM, four modes located at the far corners of 3 × 3 map were considered as dominant modes. Note that the four modes had distinct characteristics of moisture supply in both the horizontal (Fig. 2) and the vertical structure (Fig. 6). The moisture flux convergence anomalies resembled precipitation field. In the Meiyu–Baiu mode, the strong moisture flux convergence attributed to the anomalous cyclonic circulation at the low-level. The circulation had an influence on the precipitation region near southern Japan. Compared to the Meiyu–Baiu mode, the Changma mode was characterized by southwesterly moisture transport involving a large amount of moisture along the WNPSH. The post-Changma mode had a meridionally oriented moisture source over the Korean Peninsula. From various standpoints, this mode seemed to involve enhanced rainfall on the WNPSH. The characteristics of the enhanced rainfall over the WNPSH were related to the WNPSM and the TC effect in August. A dry condition over the East Asian region was shown in the dry-spell mode with the result that was caused the anomalous easterly flow at the mid-latitudes. In terms of the moisture budget equation, the major modes tended to be dominated by the anomalous moisture convergence along the rain band. A striking difference appeared in terms of the advection. The Changma and dry-spell modes were substantially affected by the advection, while the Meiyu–Baiu and post-Changma modes were weakly influenced by the effect (Fig. 4). The noticeable contributions of the advection explained localized rainfall over the Korean Peninsula in the Changma mode. Moreover, the transient eddies were found to play as opposite role in supplying or blocking the moisture.

Here we investigated the differences in thermodynamic characteristics and their instability with dynamics (Figs. 6,

7). First, the Meiyu–Baiu mode was a precipitation system brought about baroclinic instability related to an anomalous meridional thermal gradient and less developed WNPSH. This was because the large meridional thermal gradient induces the strong upper-level jet due to thermal wind balance. The jet induced the secondary circulation, namely, vertical motion on the precipitation region. For these reasons, the upward motion caused by enhanced secondary circulation was located in the warm air advection region. This condition could explain warm air rising motion. The mode was more associated with the mid-latitude system itself than with the tropical-subtropical system. The Changma mode was strongly related to the tropical-subtropical system with a well-organized WNPSH and an easterly wind shear over the tropics. This mode developed the strong convective instability (Fig. 8d), which comes from the combination by the low-level warm advection with moist from the subtropics and the upper-level cold advection with dry air from the mid-latitude. Moreover, we observed the weak secondary circulation caused by the weak upper-level zonal wind. The third mode was related to copious rain over the Korean Peninsula, which is called as the post-Changma mode. The post-Changma mode was affected by warm advection in the whole atmosphere as the Meiyu–Baiu mode, but the center of specific humidity was concentrated in the low-level as it was in the Changma mode. For these reason, this mode had intermediate features between the Meiyu–Baiu and Changma modes. From different point of view, both the anomalous moisture flux convergence and cyclonic circulation over the subtropics were indicated as the WNPSM. The fourth mode was situated diagonally opposite the Changma mode and it was referred to as the dry-spell phase, because EASM region experienced a dry condition. This was because the low-level cold advection with dry air and upper-level warm advection. The vertical conditions made the atmosphere more stable.

What caused the differences among the dominant modes? The differences might come from asymmetric responses to the ENSO to modulate the prediction of monsoon. Hence, we considered that variations in external components including the ENSO, IO, and WP could be used to predict the irregular ISO of the EASM precipitation. During the evolution of the ENSO, the thermal states of the IO and WP modulated the dependence of the intraseasonal modes on the ENSO through the WNPSH strength, easterly wind shear, and other links of the tropical-subtropical systems. The Meiyu–Baiu mode had a weakly positive correlation with the EP SST. However, the Changma mode was very sensitive to seasonal evolution of the ENSO through the IO warming and WP cooling. The condition could contribute to the maintenance of the WNPSH. The anomalous WNPSH was attributed to local air-sea interactions, the influence of the IO, and the combined effect on atmospheric circulation (Ashok et al. 2001; Saji and Yamagata 2003; Xie et al. 2009). The occurrence of the Changma mode tended to be remarkably influenced by the preceding El Niño and La Niña events, where it increased and decreased, respectively. The post-Changma mode indicated the decaying phase of the La Niña. This was the same result as that obtained by Chou et al. (2003), who showed that a strong WNPSM tended to occur in the decaying year of the La Niña. The dry-spell mode was also observed to be related with the La Niña events. In particular, the characteristics of this mode were more related to the Atlantic Ocean and IO than the others. The El Niño events had a strong impact on the IO SST, especially over the northern IO and Bay of Bengal. However, the La Niña events had weaker SST teleconnections over the same region. As a consequence, the teleconnection patterns from the tropics to mid-latitudes were observed to be quite weak during the La Niña events. The atmospheric circulation patterns, caused by the distinct influence of SST, showed the asymmetric structure and that demonstrated the asymmetric relationship between each intraseasonal mode and the ENSO.

The results have an impact on ability to classify the dominant modes in terms of the moisture supply and mechanisms by the preceding ENSO. This is important to aid in understanding the mechanisms and physical processes that govern the monsoon variability. For the better understanding of the dominant modes, the future changes and further numerical modeling works would be valuable in this regard.

Appendix: Self-organizing map (SOM) method

The SOM algorithm developed by Kohonen (1990) is a clustering algorithm used in artificial neural networks. This clustering is done without any prior information or supervision and the algorithm uses the similarity of information provided by the data to analyze differences between groups. There are two layers: the input layer and the competitive layer. All connections within the input layer are fully connected to the competitive layer. The two processes of SOM are those of training and mapping. The ability of SOM to extract patterns exists in the training algorithm.

The competitive training algorithm used was as follows.

Step 1: Initialize the connections between input vectors and nodes in the competitive layer

Step 2: Present new input vectors

Step 3: Calculate the Euclidean distances (EUD) between the input vectors and nodes in the competitive layer

The reference vector W_j is any jth node in the competitive layer. The "i" indicates the iterative process. It means that the iterative process is continued n, which indicates the number of input vector. The EUD between the reference vector W_j and the input vector X is

$$\text{EUD} = \left| X - W_j \right| = \sqrt{\sum_{i=1}^{n} (X_i - W_{ij})^2}.$$

Step 4: Select the smallest EUD to define the winning node (or best-matching node)

Step 5: Update the reference vector and adjust its associated weights together with those of the neighboring nodes within the neighborhood radius

Step 6: Continue n times. The updating equations take the form of

$$W_j(n+1) = \begin{cases} W_j(n) + c(n)\left[X(n) - W_j(n)\right], & j \in R_j(n) \\ W_j(n), & \text{otherwise} \end{cases}$$

where $X(n)$ is the input vector, $R_j(n)$ is the predefined neighborhood around node j, and $c(n)$ is the neighborhood kernel that defines the neighborhood.

The neighborhood kernel may be a monotonically decreasing function of n ($0 < c(n) < 1$), known as a bubble, or it may be a function of the Gaussian type. We used the latter, which was expressed as

$$\alpha(n) \exp\left[\frac{-\left\| r_j - r_i^2 \right\|}{2\sigma^2(n)}\right]$$

where $\alpha(n)$ and $\sigma(n)$ are constants that linearly decrease with n. Here, $\alpha(n)$ is the learning rate, which determines the speed of the learning process, while $\sigma(n)$ is the amplitude, which determines the width of the neighborhood kernel. In addition, r_j and r_i are the coordinates of the nodes j and i, respectively, for which the neighborhood kernel is defined.

Step 7: Determine the winning node with the least EUD between itself and the input vector after the nodes are randomly distributed

Step 8: Distribute each input vector to a corresponding reference vector based on its similarity in terms of a criterion such as the least EUD

Step 9: Represent the particular input sample (mapping process) most effectively. The number of output patterns is defined by the user

Moisture budget equation

The equation of conservation of water vapor and the equation of continuity are (Trenberth and Guillemot 1995)

$$\frac{\partial q}{\partial t} + \mathbf{V} \cdot \nabla q + \omega \frac{\partial q}{\partial p} = e - c \tag{2}$$

$$\nabla \cdot \mathbf{V} + \frac{\partial \omega}{\partial p} = 0 \tag{3}$$

The precipitation rate on the right-hand side of Eq. (2) is determined by the rate of re-evaporation, e, and the rate of condensation per unit mass, c. The role of liquid water in the atmosphere is ignored. If Eq. (3) is used, then Eq. (2) can be expressed in flux form as

$$\frac{\partial q}{\partial t} + \nabla \cdot (\mathbf{q}\mathbf{V}) + \frac{\partial}{\partial p}(q\omega) = e - c \tag{4}$$

Using the generic relationships for q yields

$$\int_0^{p_s} \frac{\partial q}{\partial t} dp = \frac{\partial}{\partial t} \int_0^{p_s} q dp - q_s \frac{\partial p_s}{\partial t} \tag{5a}$$

$$\int_0^{p_s} \nabla \cdot (q\mathbf{V}) dp = \nabla \cdot \int_0^{p_s} (qV) dp - q_s \mathbf{V_s} \cdot \nabla p_s \tag{5b}$$

$$\int_0^{p_s} \frac{\partial(q\omega)}{\partial p} dp = q_s \omega_s = q_s \left(\frac{\partial p_s}{\partial t} + \mathbf{V_s} \cdot \nabla p_s \right) \tag{5c}$$

The vertically integrated equation Eq. (4) can be written as

$$\int_0^{p_s} \frac{\partial q}{\partial t} dp + \int_0^{p_s} \nabla \cdot \mathbf{q}\mathbf{V} dp + \int_0^{p_s} \frac{\partial}{\partial p} q\omega dp = \rho_w \mathrm{g}(E - P) \tag{6}$$

and then Eqs. (5a–5c) are substituted into Eq. (6).

$$\frac{\partial}{\partial t} \int_0^{p_s} q dp - q_s \frac{\partial p_s}{\partial t} + \nabla \cdot \int_0^{p_s} (qV) dp - q_s \mathbf{V_s} \cdot \nabla p_s + q_s \frac{\partial p_s}{\partial t}$$
$$+ q_s \mathbf{V_s} \cdot \nabla p_s = \rho_w \mathrm{g}(E - P) \tag{7}$$

Since the change of moisture in the atmosphere is small, the first term on the left-hand side of Eq. (7) can be neglected. The moisture flux can be separated into two parts: the stationary component and the transient component. Hence, we prescribed that an overbar indicates a 15-day running mean and a prime denotes the departure from that 15-day running mean, so that

$$\mathbf{V} = \overline{V} + V'$$

Similarly, the moisture flux can be expressed as $\overline{qV} = \overline{q}\,\overline{V} + \overline{\overline{q}V'} + \overline{q'\overline{V}} + \overline{q'V'}$.

The second and third terms on the right-hand side approximately vanish and were not considered. Thus, the final moisture budget equation was derived by taking a time average as follows:

$$\rho_w g(P - E) \cong - \int_0^{P_s} \left(\overline{q} \nabla \cdot \overline{V} + \overline{V} \cdot \nabla \overline{q} \right) dp - \int_0^{P_s} \nabla \cdot \left(\overline{V'q'} \right) dp \qquad (8)$$

where $\overline{V}$ is the horizontal wind vector and q is specific humidity. On the right-hand side of Eq. (8), the two terms in the first integral describe the moisture convergence and the moisture advection by the mean flow, respectively. The second term describes the moisture flux convergence by transient eddies.

References

Ashok K, Guan Z, Yamagata T (2001) Impact of the Indian Ocean dipole on the relationship between the Indian monsoon rainfall and ENSO. Geophys Res Lett 28:4499–4502

Chang CP, Zhang YS, Li T (2000) Interannual and interdecadal variations of the East Asian summer monsoon and tropical Pacific SSTs. Part I: roles of the subtropical ridge. J Clim 13:4310–4325

Chattopadhyay R, Sahai AK, Goswami BN (2008) Objective Identification of nonlinear convectively coupled phases of monsoon intraseasonal oscillation: implications for prediction. J Atmos Sci 65:1549–1569

Chou C, Tu JY, Yu JY (2003) Interannual variability of the western north Pacific Summer monsoon: differences between ENSO and Non-ENSO years. J Clim 16:2275–2287

Chu JE, Ha KJ (2011) Classification of intraseasonal oscillation in precipitation using self-organizing map for the East Asian summer monsoon. Atmos Krn Meteorol Soc 21:221–228

Chu JE, Saji NH, Ha KJ (2012) Non-linear, intraseasonal phases of the East Asian summer monsoon: extraction and analysis using self-organizing maps. J Clim 25(20):6975–6988. doi:10.1175/JCLI-D-11-00512.1

Enomoto T, Hoskins BJ, Matsuda Y (2003) The formation mechanism of the Bonin high in August. Q J R Meteorol Soc Jpn 129:157–178

Ha KJ, Lee SS (2007) On the interannual variability of the Bonin high associated with the East Asian summer monsoon rain. Clim Dyn 28:67–83. doi:10.1007/s00382-006-0169-x

Ha KJ, Park SK, Kim KY (2005) On interannual characteristics of climate prediction center merged analysis precipitation over the Korean peninsula during the summer monsoon season. Int J Climatol 25:99–116. doi:10.1002/joc.1116

Ha KJ, Yun KS, Jhun JG, Li J (2009) Circulation changes associated with the interdecadal shift of Korean August rainfall around late 1960s. J Geophys Res 114:D04115. doi:10.1029/2008JD011287

Huang RH, Wu YF (1989) The influence of ENSO on the summer climate change in China and its mechanism. Adv Atmos Sci 6:21–32

Jiang X, Li T, Wang B (2004) Structures and mechanisms of the northward propagating boreal summer intraseasonal oscillation. J Clim 17:1022–1039

Johnson N (2013) How many ENSO flavors can we distinguish? J Clim 26:4816–4827

Kanamitsu M, Ebisuzaki W, Woollen J, Yang SK, Hnilo JJ, Fiorino M, Potter GL (2002) NCEP-DOE AMIP-II reanalysis (R-2). Bull Am Meteorol Soc 83:1631–1643

Kang IS, Ho CH, Lim YK (1999) Principal modes of climatological seasonal and intraseasonal variations of the Asian summer monsoon. Mon Weather Rev 127:322–340

Karori MA, Li J, Jin FF (2013) The asymmetric influence of the two types of El Niño and La Niña on summer rainfall over southeast China. J Clim 26:4567–4582

Kemball-Cook S, Wang B (2001) Equatorial waves and air–sea interaction in the boreal summer intraseasonal oscillation. J Clim 14:2923–2942

Kim HM, Kang IS, Wang B, Lee JY (2008) Interannual variations of the boreal summer intraseasonal variability predicted by ten atmosphere-ocean coupled models. Clim Dyn 30:485–496

Kim KY, Roh JW, Lee DK, Jhun JG (2010) Physical mechanisms of the seasonal, subseasonal, and high-frequency variability in the seasonal cycle of summer precipitation in Korea. J Geophys Res 115:D14110. doi:10.1029/2009JD013561

Kohonen T (1990) The self-organizing map. Proc IEEE 78:1464–1480

Kwon MH, Jhun JG, Ha KJ (2007) Decadal change in East Asian summer monsoon circulation in the mid-1990s. Geophys Res Lett 34:L21706. doi:10.1029/2007GL031977

Lau KM, Kim KM, Yang S (2000) Dynamical and boundary forcing characteristics of regional components of the Asian summer monsoon. J Clim 13:2461–2482

Lee SS, Vinayachandran PN, Ha KJ, Jhun JG (2010) Shift of peak in summer monsoon rainfall over Korea and its association with El Niño-southern oscillation. J Geophys Res 115:D02111. doi:10.1029/2009JD011717

Lee EJ, Ha KJ, Jhun JG (2013a) Interdecadal changes in interannual variability of the global monsoon precipitation and interrelationships among its subcomponents. Clim Dyn. doi:10.1007/s00382-013-1762-4

Lee SS, Seo YW, Ha KJ, Jhun JG (2013b) Impact of the western North Pacific subtropical high on the East Asian monsoon precipitation and the Indian Ocean precipitation in the boreal summertime. Asia-Pac J Atmos Sci 49(2):171–182. doi:10.1007/s13143-013-0017-y

Li L, Li W, Barros AP (2013) Atmospheric moisture budget and its regulation of the summer precipitation variability over the Southeastern United States. Clim Dyn 41:613–631

Lindzen RS, Farrell B (1980) A simple approximate result for the maximum growth rate of baroclinic instabilities. J Atmos Sci 37:1648–1654

Nakamura H (1992) Midwinter suppression of baroclinic wave activity in the Pacific. J Atmos Sci 49:1629–1642

Nitta T (1987) Convective activities in the tropical western Pacific and their impact on the Northern Hemisphere summer circulation. J Meteorol Soc Jpn 65:373–390

Rayner NA, Parker DE, Horton EB, Folland CK, Alexander LV, Rowell DP, Kent EC, Kaplan A (2003) Global analyses of sea surface temperature, sea ice, and night marine air temperature since the late nineteenth century. J Geophys Res 108(D14):4407

Saji NH, Yamagata T (2003) Possible impacts of Indian Ocean dipole mode events on global climate. Clim Res 25:151–169. doi:10.3365/cr025151

Sanjib KK, Ha KJ (2003) Characteristic differences of rainfall and cloud-to-ground lightning activity over south Korea during the summer monsoon season. Mon Weather Rev 131:2312–2323

Seager R, Naik N, Vecchi GA (2010) Thermodynamic and dynamic mechanisms for large-scale changes in the hydrological cycle in response to global warming. J Clim 23:4651–4668

Seo KH, Son JH, Lee SE, Tomita T, Park HS (2012) Mechanisms of an extraordinary East Asian summer monsoon event in July 2011. Geophys Res Lett 39:L05704

Teng H, Wang B (2003) Interannual variations of the boreal summer intraseasonal oscillation in the Asian-Pacific region. J Clim 16:3572–3584

Trenberth K, Guillemot CJ (1995) Evaluation of the global atmospheric moisture budget as seen from analyses. J Clim 8:2255–2272

Tsou CH, Hsu PC, Kau WS, Hsu HH (2005) Northward and northwestward propagation of 30–60 day oscillation in the tropical and extratropical western North Pacific. J Meteorol Soc Jpn 83:711–726. doi:10.2151/jmsj.83.711

Wang B, Xu X (1997) Northern Hemisphere summer monsoon singularities and climatological intraseasonal oscillation. J Clim 10:1071–1085

Wang Q, Ding Y, Jiang Y (1998) Relationship between Asian monsoon activities and the precipitation over China mainland. Quart J Appl Meteorol 9:84–89

Wang B, Wu R, Fu X (2000) Pacific-East Asia teleconnection: how does ENSO affect East Asian climate? J Clim 13:1517–1536

Wang B, Wu R, Lau KM (2001) Interannual variability of the Asian summer monsoon: contrasts between the Indian and the western north Pacific-East Asian monsoons. J Clim 14:4073–4090

Wang B, Xiang B, Lee JY (2013) Subtropical high predictability establishes a promising way for monsoon and tropical storm predictions. PNAS 110:2718–2722

Watanabe M, Jin FF (2002) Role of Indian Ocean warming in the development of Philippine Sea anticyclone during ENSO. Geophys Res Lett 29:1478. doi:10.29/2001GL014318

Wu R, Hu ZZ, Kirtman BP (2003) Evolution of ENSO related rainfall anomalies in East Asia. J Clim 16:3742–3758

Xie SP, Hu K, Hafner J, Tokinaga H, Du Y, Huang G, Sampe T (2009) Indian ocean capacitor effect on indo-western Pacific climate during the summer following El Niño. J Clim 22:730–747

Yang J, Liu Q, Xie SP, Liu Z, Wu L (2007) Impact of the Indian Ocean SST basin mode on the Asian summer monsoon. Geophys Res Lett 34:L02708

Yasunari T (1979) Cloudiness fluctuations associated with the Northern Hemisphere summer monsoon. J Meteorol Soc Jpn 57:227–242

Yoo JH, Robertson AW, Kang IS (2010) Analysis of intraseasonal and interannual variability of the Asian summer monsoon using a hidden Markov model. J Clim 23:5498–5516

Yun KS, Seo KH, Ha KJ (2008) Relationship between ENSO and northward propagating intraseasonal oscillation in the East Asian summer monsoon system. J Geophys Res 113:D14120. doi:10.1029/2008JD009901

Yun KS, Ren B, Ha KJ, Chan JCL, Jhun JG (2009) The 30–60-day oscillation in the East Asian summer monsoon and its time-dependent association with the ENSO. Tellus 61A:565–578. doi:10.1111/j.1600-0870.2009.00410.x

Yun KS, Yeh SW, Ha KJ (2013) Distinct impact of tropical SSTs on summer North Pacific high and western North Pacific subtropical high. J Geophys Res Atmos 118:4107–4116. doi:10.1002/jgrd.50253

Zhang KJ, Dai XG, Wang P (2011) East Asian precipitation pattern: competition between monsoon and transient eddies. Chin J Geophys 54(6):870–882

Zhou TJ, Yu RC (2005) Atmospheric water vapor transport associated with typical anomalous summer rainfall patterns in China. J Geophys Res 110:D08104. doi:10.1029/2004JD005413